nature photonics

SUPPLEMENTARY INFORMATION

DOI: 10.1038/NPHOTON.2014.1

Voltage-switchable photocurrents in single-wall carbon nanotube – silicon junctions for analogue and digital optoelectronics

Young Lae Kim,[1] Hyun Young Jung,[1] Sora Park,[2] Bo Li,[1] Fangze Liu,[3] Ji Hao,[1] Young-Kyun Kwon,[2,*] Yung Joon Jung,[1,2,*] and Swastik Kar[3,*]

[1]*Department of Mechanical and Industrial Engineering, Northeastern University, Boston, Massachusetts 02115, USA,* [2]*Department of Physics and Research Institute for Basic Sciences, Kyung Hee University, Seoul, 130-701 Korea,* [3]*Department of Physics, Northeastern University, Boston, Massachusetts 02115, USA.*

*Corresponding Author(s): E-mails: ykkwon@khu.ac.kr(YKK); jungy@coe.neu.edu(YJJ); s.kar@neu.edu(SK)

Supplementary Information

S1: Characterizations of the commercially purchased SWNTs

The SWNT-DI (de-ionized) water dispersion (concentration of 0.23 wt %) was purchased from *Brewer Science* Inc. (CNTRENE™ C100). The nanotubes were CVD grown and of mixed chirality in nature. The typical length of the SWNTs was specified to be between 0.8 μm and 1μm, with an average diameter of about 1nm. Our own AFM and Raman spectroscopy measurements were mostly in agreement with about ~10% deviation in specified length range and diameter. The vendor specified that they have not purified the SWNTs, and the dispersion was a mixture containing a natural ratio of metallic and semiconducting nanotubes, which can be assumed to be approximately 2/3rd semiconducting and 1/3rd metallic in nature. This is consistent with our UV-visible absorption spectroscopy characterizations, as shown in section S1.4. The following characterizations were performed on these SWNTs samples:

S1.A Contact angle measurement: Contact angle measurement was performed using Phoenix 150 contact angle measurement system (Surface Electro Optics Co., Ltd.). The as-received SWNTs were found to remain stably suspended DI water owing to its slightly hydrophilic nature, and we confirmed this by performing contact-angle measurement of DI water on an assemble mat which was thoroughly rinsed. Figure S1.1 shows the digital image of a water droplet forming a contact angle of ~38°.

DOI: 10.1038/NPHOTON.2014.1

The vendor specified that the hydrophilic nature of the nanotubes was obtained not by using any surfactants, but through a proprietary method that attaches carboxylic functional groups to the SWNTs. From this, we assume that the nanotubes may have been purified using a long-term acid-treatment method that often introduces defects sites onto which –COOH and other polar functional groups get attached, rendering them slightly hydrophilic.[Footnote 1]

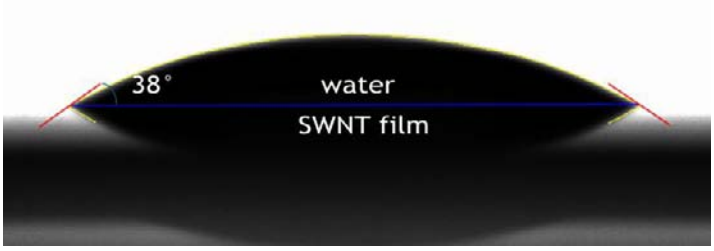

Figure S1.1: *Contact angle measurement of a drop of water placed on a densely packed SWNT film assembled on a SiO_2 surface showing a contact angle of 38°, revealing their slightly hydrophilic nature.*

S1.B XPS of the SWNTs: X-ray photoelectron spectroscopy (XPS) was performed using PHI Quantera XPS (Physical Electronics, Inc.). Films of SWNTs were assembled on Si substrate with 100 nm thick SiO_2 through the method of fluidic guided assembly. The photoresist (S1805) was stripped off completely using hot acetone (70 °C) followed by rinsing in fresh IPA using

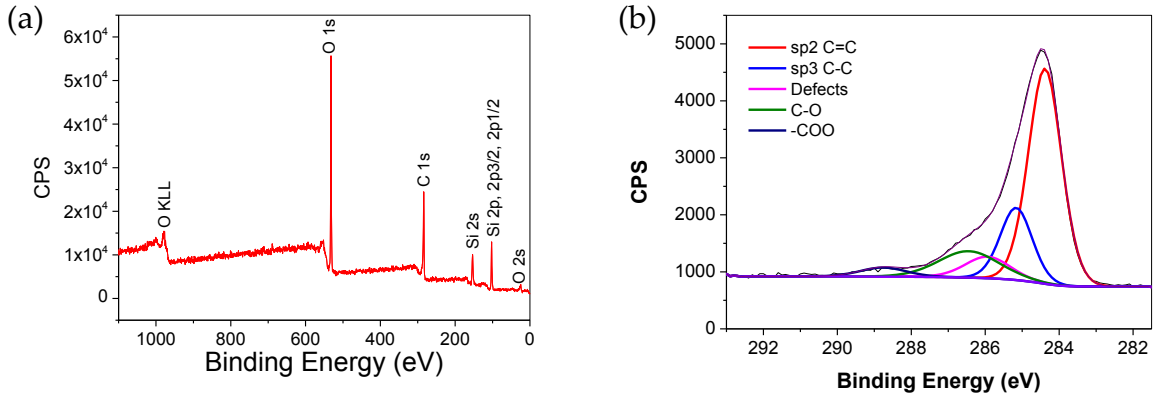

Figure S1.2: *XPS spectrum of SWNT film on SiO_2/Si substrate: survey scan (a) and XPS C1s spectrum (b). The fit to (b) is obtained by adding a sp^2 C=C peak, a sp^3 C-C peak, a defect peak, a C-O peak and a –COO peak centered at 284.38 eV, 285.16 eV, 285.94 eV, 286.45 eV and 288.83 eV, respectively.*

Footnote 1: This purification process is commonly used for dissolving the catalyst nanoparticles and other impurities from CVD-grown single-wall carbon nanotubes, as also to "cut" carbon nanotubes, see "Fullerene pipes" Science 280, 1253 (1998), and "Large-scale purification of single-wall carbon nanotubes: process, product, and characterization" Appl. Phys. A 67, 29-37 (1998). Although this process is known to partially p-dope the SWNTs (see Tey *et al.*, *Nanoscale Research Letters* **7**, 548 (2012), we find that such doping, if any, does not affect the rectification behaviour of their junction with p–Si, which still have reasonably high turn-on voltages, see figure S4.1

processes developed exclusively for these SWNTs[1]. A monochromatized Al Kα X-ray source (hν=1486.7 eV) was used to perform the XPS analysis. The pass energy was 140 eV for the survey scan and 26 eV for C1s spectrum. The analyzed C1s region was limited to the binding energy interval from 281.5 to 293 eV. Figure S1.2 shows the survey scan and C1s spectrum of the SWNTs. From this, the following bonds were assigned according to the references[2]: sp^2 C=C (284.38–284.53 eV), sp^3 C–C (285.11–285.5eV), C–O (286.21–287.53eV), >C=O (286.45–287.92 eV), -COO (288.39–289.54eV). The peak at 285.9 was assigned as a defect peak[3]. The relative presence of various bond types has been tabulated in table S1.1.

Bond	Position	FWHM	Area	% Conc.
sp^2 C=C	284.38	1.06	4325.1	57.51
sp^3 C-C	285.16	1.016	1397.5	18.58
Defect	285.94	1.426	584.7	7.77
C-O	286.45	1.91	961.6	12.78
-COO	288.83	1.46	252.5	3.36

Table S1.1 *Details of the C1s peak-deconstruction*

S1.C Raman Spectroscopy (LabRAM HR 800, Horiba Jobin Yvon)**:** Raman spectra of the SWNTs (assembled on a SiO_2/Si wafer) were measured with a 532 nm (2.33 eV) laser line. Figure S1.3a shows a typical Raman spectrum featuring the well-known G and G′ peaks, which are signature peaks of graphitic carbon systems such as carbon nanotubes. Also seen in this figure is the

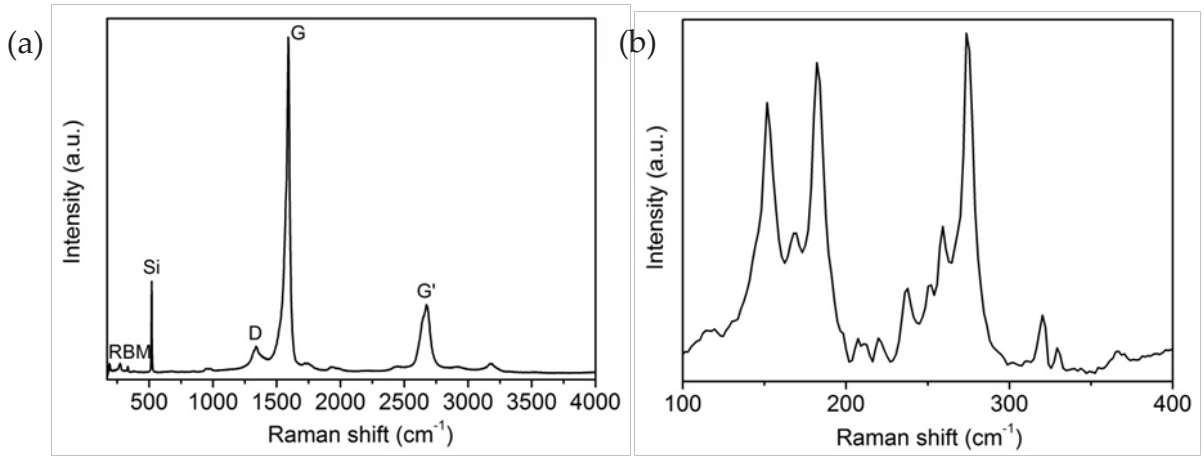

Figure S1.3: *Typical Raman Spectrum of the SWNTs (a) Full spectrum showing the well-known G and G′ peaks, along with a small D-peak, which appears from defects. Low-intensity peaks at the low-Raman shift values (up to a few 100 cm^{-1}) are the Radial breathing modes, which are unique signatures of single-wall nanotubes (see text).*

DOI: 10.1038/NPHOTON.2014.1

defect-induced D band, its presence being consistent with the presence of a defect peak in the XPS spectrum. SWNTs, due to their extremely narrow diameter, also exhibit certain radial breathing modes, which typically appear at Raman shift values of a few 100 cm^{-1}. The positions of these peaks are diameter dependent. Figure S1.3b shows an array of peaks representing the radial breathing modes of SWNTs that lie within the excitation spot of the Raman laser.

S1.D UV-Visible Absorption spectroscopy: [Perkin Elmer Lambda 35 UV/Vis spectrophotometer]: Optical absorption (300 nm <λ <1100 nm) measurements were performed on thin films of SWNTs transferred onto a transparent polymer (poly-dimethylsiloxane, PDMS) substrate, with the background absorbance due to pure PDMS carefully subtracted via a control run under similar conditions. The featureless slowly-varying broadband absorbance is similar to that reported for unsorted HiPco SWNTs of mixed chiralities, and unlike those of enriched SWNTs.[4]

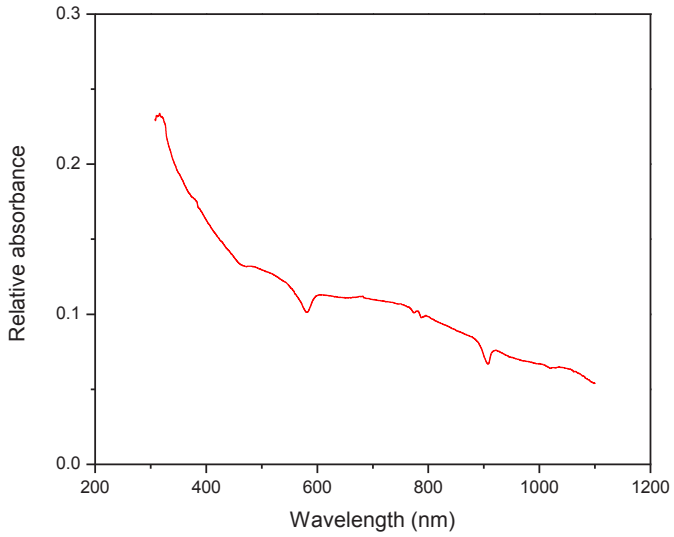

Figure S1.4: *Background subtracted UV-visible absorption spectrum of a thin film of SWNTs transferred onto a transparent polymer surface (Polydimethylsiloxane, or PDMS).*

S1.E Sheet Resistance:[Keithley Model 2400 Sourcemeter] The sheet resistance of SWNT films assembled under the same conditions as described in section S2 was measured using a sourcemeter. Belts of SWNTs (1-2 micron wide, and several microns long) were assembled on a SiO_2/Si substrate and lithographically contacted with Ti/Au electrodes. The SWNT resistance

and interfacial contact resistance were separately measured using approaches described in reference[1]. The measured nominal sheet resistance R_{sheet} (after subtracting the interfacial contact resistance of the electrical leads) was found to lie between 300 Ω/□ < R_{sheet}<400 Ω/□.

S2. Fabrication of SWNT/Si devices: P-type Si wafer (resistivity in the range of 1-10 Ω-cm) with 300-nm thick SiO_2 layer was purchased from University Wafer, Inc.

S2.A Silicon surface preparation: The as-received wafers was protected by photoresist (S1813, MicroChem Corp) and then cut into the desired shape (chips) using a dicing saw. The photoresist was stripped off using hot acetone followed by rinsing in IPA. To further remove any possible organic contaminations, the chips were emerged in the piranha solution (H_2SO_4:H_2O_2=2:1) at elevated temperature (105 °C) for at least 10 min, followed by rinsing in the DI water for another 10 to 15 min. The oxide was then removed after lithographically patterning the area using buffered HF (BOE) to expose fresh Si surface in pre-destined locations for subsequent SWNT deposition. The fresh exposed Si surface was rinsed in DI water for 10 to 15 min to remove HF residue. The photoresist was stripped off using hot acetone (70-80 °C) followed by rinsing in IPA and drying in N_2. After that, a surface treatment was conducted using plasma (O_2 (20 sccm), SF_6 (20 sccm) and Ar (5 sccm)) for 3-5 seconds to enhance the affinity of Si and SiO_2 surface to water based SWNT solution[5-7]. The plasma treatment further cleans the Si surface.

S2.B. SWNT assembly for test structure and logic devices: Immediately after the surface treatment, a well-established guided fluidic assembly process of SWNT was used to assemble SWNTs on the desired surface with a prescribed set of assembly steps[5-7]. To prepare the devices show in figure 1, 3 and 4, the prepared substrate was spin-coated with a photoresist film and patterned using photolithography. Patterned substrate was vertically submerged into the SWNT-DI water solution using a dip-coater and gradually lifted from the solution with a constant pulling speed of 0.1 mm·min^{-1}. Two dip-coating processes with 180 degree rotation were applied to make a better, more uniform coverage of SWNTs along the trenches between patterned photoresist. After this assembly process, the photoresist film was removed in acetone and rinsed in DI water. Then, the substrate was dried with nitrogen. For electrical

DOI: 10.1038/NPHOTON.2014.1

characterization, contact pads were fabricated on the surface of SWNTs and oxide substrate using an optical lithography and Ti (5 nm)/Au (150 nm) deposition followed by a lift-off process. To make an Ohmic contact between Ti/Au and Si surface in the area without SWNTs, the Si surface was scratched gently right before the deposition of Ti/Au electrodes. The electrical characterization was conducted using a Janis ST-500 electrical probe station connected to an Agilent 4156C precision semiconductor parameter analyzer. Care was taken to complete these steps in a timely manner, such that SWNTs are assembled directly on a fresh-exposed p-Si surface with minimum formation of native oxide. In addition, the absence of any surfactants implied a direct access of the SWNTs at the junction area.

After SWNT deposition, a standard photolithography process was utilized to define the metal contact pads for electrical measurement. The metal deposition (Ti/Au = 5 nm/150 nm) was performed using MRC 8667 sputtering system. The devices was further stripped by hot acetone and rinsed by fresh IPA for multiple times to fully remove the photoresist residue.

S2.C SWNT assembly for the photodetector array (figure 2): Each detector in the array contains an isolated 15×15 μm^2 fluidically-assembled SWNT film conformally overlaid onto a 5-μm-diameter Si window etched out of a 300-nm thick SiO_2 layer. Fabrication of the detector array was accomplished through a complex three-mask lithography process, one each for etching Si windows, depositing SWNT films, and fabricating electrodes. Firstly, a 300-nm thick SiO_2 substrate was spin-coated with a photoresist film and patterned with circular openings using an optical lithography. With this first mask process, an array of 250,000 holes (500 by 500) was defined on a 12×12mm^2 area SiO_2/Si chip. The patterned chip was etched by BOE 10:1 solution for 9 min. to expose circular Si surfaces (see Figure S2.1 (a and b)). Then, to improve the quality of assembly of SWNTs, the substrate was pretreated using the same plasma treatment described earlier. Next, the second mask process was conducted for the SWNTs assembly followed by another optical lithography (see Figure S2.1(c and d)). The patterned substrate was vertically submerged into the SWNT-DI water solution using a dip-coater and gradually lifted from the solution with a constant pulling speed of 0.1 $mm \cdot min^{-1}$. Four dip-coating processes with 90 degree rotation each time were applied to obtain a uniform coverage of SWNTs within

the square patterns (see Figure S2.1 (e and f)). After this assembly process, the photoresist film was removed in acetone and rinsed in DI water. Then, the substrate was dried with nitrogen.

For the metal electrodes, a third mask process was conducted, followed by another optical lithography step to open a boundary area between SWNTs and SiO_2 surface (see Figure S2.2(a and b)). Then, contact pads were fabricated on the surface of SWNTs and oxide substrate with Ti (5 nm)/Au (150 nm) deposition followed by a lift-off process (see Figure S2.2(c and d)). The finished device comprised of an array of 250,000 holes on a 12×12mm^2 area SiO_2/Si chip, designed to mimic the front-end of a 0.25 Megapixel focal plane array. Each sensor contained an isolated 15×15 μm^2 assembled SWNT film overlaid onto a 5-μm-diameter Si window etched out of a 300-nm thick SiO_2 layer.

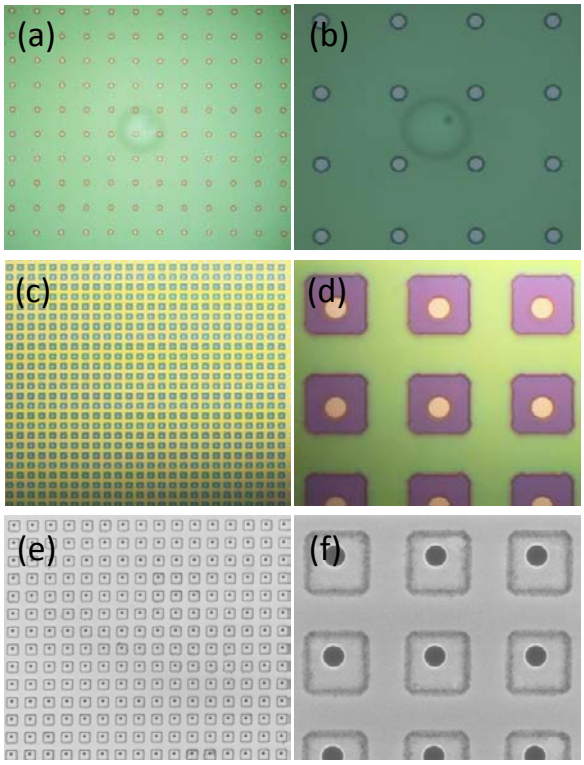

Figure S2.1 *Optical and SEM images of Si hole and SWNT assembly for very-large scale sensor array. (a and b) Optical images of etched Si surface with 5 μm diameter holes (green color: SiO_2, gray color: Si). (c and d) Optical images after the first mask process (green color: photoresist, purple color: SiO_2, orange color: Si surface). (e and f) SEM images after assembly of SWNTs.*

DOI: 10.1038/NPHOTON.2014.1

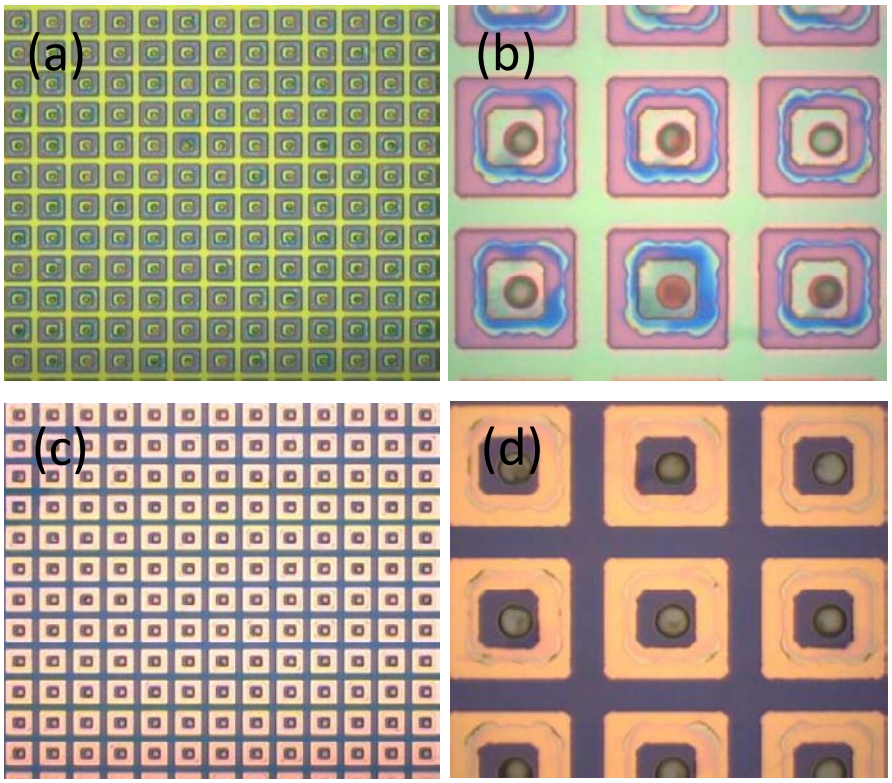

Figure S2.2. *Optical images of assembled SWNTs and electrodes. (a and b) Optical images after the second mask process for electrodes (green color: photoresist, purple color: SiO_2, blue color: SWNTs). (c and d) Optical images with electrodes of Ti/Au (yellow color: Au, purple color: SiO_2, assembled SWNTs on holes).*

In addition to the assembled pixel array, a separate, 10x10 array of photodetector array was fabricated with the electrical lead (Ti/Au) shorted to an external contact pad, for testing the uniformity of photocurrent response. Figure S2.3 shows such a test-structure device.

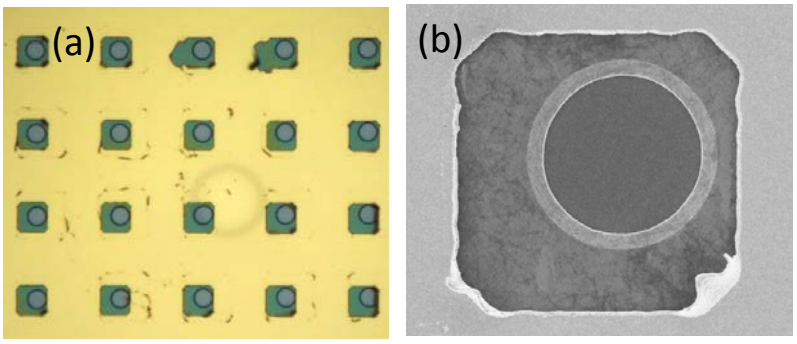

Figure S2.3. *(a) Digital photograph and (b) SEM image of a test-structure sensor array for photocurrent mapping measurement*

S3. Possible role of native oxide on the junction resistance: Despite our best efforts to completely remove the SiO_2 coating and keep the Si surface clean before and during the SWNT assembly, it is very likely that native oxides (typically up to a nanometer thin, when exposed to air) do reform on Si. This is especially so since we do not expect the SWNTs to form any chemical bonds with Si. Hence, in order to model the junction, it is important to examine whether this native oxide layer significantly affects the junction series resistance, or remains as a passive tunneling barrier. In order to ascertain that, we note that in a conventional diode with a series resistance, R_S, the I-V equation gets modified to the following equation:

$$I(V,I) = I_s(e^{q(V-IR_S)/nk_BT} - 1).$$

This can be re-written for the voltage, V, in the form:

$$V(I) = (nk_BT/q) \times \ln(I/I_s + 1) + IR_S.$$

Taking the first derivative, and multiplying throughout by I, we obtain:

$$I[\frac{dV}{dI}] = \frac{(nk_BT/q)}{(1 + I_s/I)} + IR_S.$$

At higher forward bias regions, where I>>Is, this equation simplifies to:

$$I[\frac{dV}{dI}] = \frac{nk_BT}{q} + IR_S.$$

Hence, the slope of $I(dV/dI)$ *vs.* I at high forward bias currents gives R_S. Figure S3.1a shows the linear fit to the high-current region of the forward bias-current in a device whose structure is shown schematically in Figure S3.1b. The estimated value of series resistance from this graph is $R_S = 32k\Omega$.

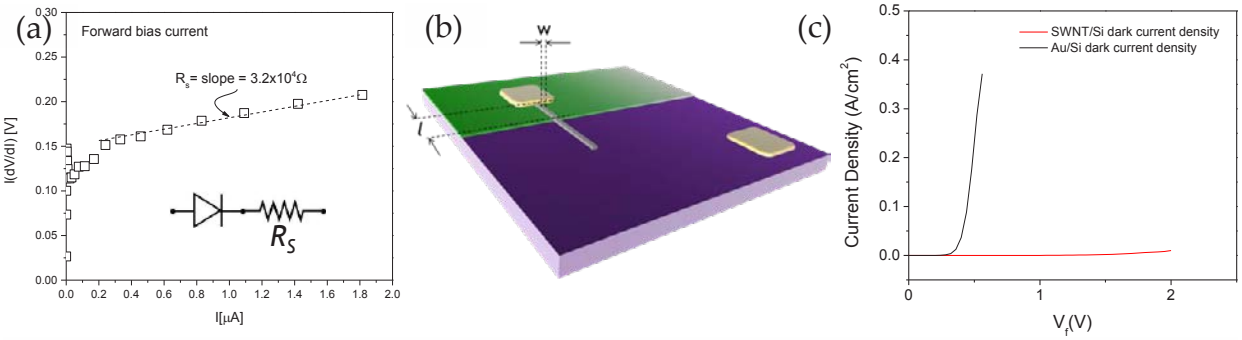

Figure S3.1: *(a) Estimation of the series resistance from the forward bias current (see text). (b) Dimensions of the nanotube belt that provides an additional resistance in series with the device. (c) Comparative current densities in the Au/Si and SWNT/Si junctions.*

If we assume that this value of series resistance (R_S) is largely from the portion of the SWNT belt that lies on the SiO_2 and not on Si, then the estimated sheet resistance of this region would be:

$$R_{sheet} = (\frac{w}{l})R_S ,$$

where, w and l are defined as the width and length as shown in figure S3.1b. For this device, (w/l) = (1/95)=0.0105, and hence, the estimated sheet resistance, R_{sheet} = 0.0105×32kΩ ≈320 Ω/□, which compares very nicely with the sheet resistance of the pure SWNT belt, estimated independently, as discussed in section S1.E. This seems to suggest that the overall current in the device is largely limited by the electrical property of the SWNTs (as we will see next, in particular, their low DoS near the Fermi level), and not any interfacial junction oxide barrier. We confirm this further by comparing the forward current density in the SWNT/Si junctions with that of Au/Si junctions, as shown in figure S3.1c. It is clear that at high bias, the current density is much higher in the Au/Si junction at a much lower forward bias due to the comparatively smaller sheet resistance of the Au electrode. This would not have been possible if the forward current was limited by the junction resistance of any oxide barrier, which would be similar for both Au/Si and SWNT/Si junctions.

From this, we conclude that the series resistance due to any native oxide was not significantly large, possibly playing a role of a very thin tunneling barrier. This has been included into the model described next.

S4. Non-linear photoresponse in SWNT-Si heterojunctions: A model

To understand the obtained unconventional and sharply non-linear photoresponse, we note that the electron affinity of Si χ_{Si}≈4.05eV, whereas the work-function of SWNT mats, ϕ_{SWNT} ≈ 3.7-4.4 eV,[8,9] implying that in an unbiased junction, the Fermi level of SWNTs lie close to the conduction band edge (CBE) of Si.[Footnote 2] This results in a relatively high forward turn-on voltage (V_{to}) in these junctions (V_{to} ~ 0.7-0.8V, see figure S4.1a) compared to the Au/Si junctions, where a much lower V_{to} is seen (V_{to} << 0.5V) owing to the high work-function of Au (≈ 5eV). In past reports, these junctions have been modelled in terms of a metal-semiconductor "Schottky-

Footnote 2. In analysing these junctions, we have intentionally selected the work-function values of SWNTs that are in mat-like architectures. We note that these values are lower than those reported for individual or small bundles of SWNTs as reported in [Appl. Phys. A **75**, 479 (2002)], and [Phys. Rev. B **65**, 193401 (2002)] which are architecturally dissimilar from our system.

barrier" junction, where the SWNTs are treated as passive, transparent conductive (metallic) electrodes. This simple description is inadequate in explaining the non-linear, reverse-bias dependent photocurrent seen in our devices, and the detailed electronic structure and the effective DoS of SWNT belts play a vital role. Since SWNTs have low DoS near their Fermi level, any photoexcited electrons near the CBE find very few accessible states in SWNTs to inject into, resulting in the near-zero short-circuit photocurrent seen in our devices. Under an applied reverse bias, however, the Fermi level of SWNTs gets lowered, allowing regions of high DoS (and hence, a large number of unoccupied accessible states) to align with the CBE of Si, and hence a large number of photoexcited carriers can inject into SWNTs. The photocurrent is hence limited by the number of accessible states between the position of the CBE of Si and the Fermi level of SWNTs (at $\varepsilon=eV_r$, where V_r is the reverse bias) in SWNTs, and its voltage dependence can also be expected to follow the electron-energy dependence of the number of accessible states, $n(\varepsilon=eV_r)$, obtained by integrating the SWNT DoS between $\varepsilon=0$ and $\varepsilon=eV_r$. Hence, in the first approximation, we can assume that the voltage dependence of the measured photocurrent is directly proportional (ignoring the geometry of the electrodes) to the total number of accessible states $n(\varepsilon)$ for the photoexcited carriers to inject into.

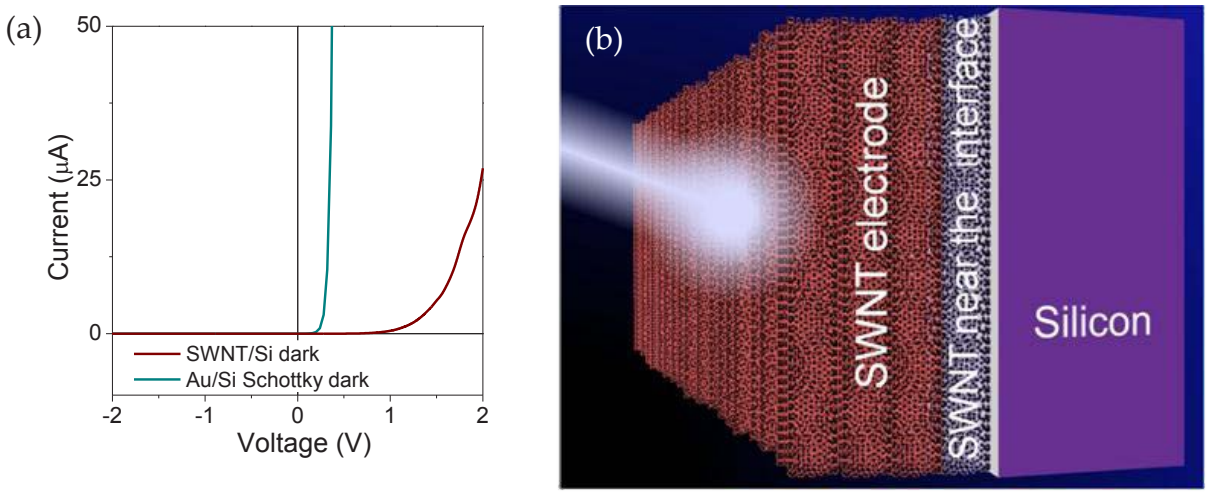

Figure S4.1: *(a) Dark currents in Au/Si Schottky and SWNT/Si junctions. (b)Schematic showing the SWNT-Si structures divided into different regions for semi-quantitative analysis.*

To obtain $n(\varepsilon)$, we assume that the heterojunction can be divided into three regions, namely the (a) the bulk Si region with a thin layer of native oxide, (b) the SWNTs at the interface, and (c)

DOI: 10.1038/NPHOTON.2014.1

the SWNT electrode, as shown in figure S4.1b. We performed *ab-initio* density functional theory (DFT) calculations to obtain the electronic structure of a typical SWNT at the Si interface, and utilized prior results published elsewhere to model the electronic structure of (c). The non-linear and voltage-dependent photocurrent has been modeled using a combination of these results. These have been presented in the next sections. Despite the simplicity of this model, we find a reasonable agreement between the electron energy (voltage) dependence of (a) the number of accessible states and (b) the photocurrent.

S4a: Ab-initio DFT modeling of SWNT-Si interface: We performed first-principle DFT calculations using SIESTA code[10] to investigate the geometrical and electronic structures of a (6,2) SWNT. Figure S4.2 shows the calculated electronic band structure and Density of States (DoS) of an isolated (6,2) SWNT.

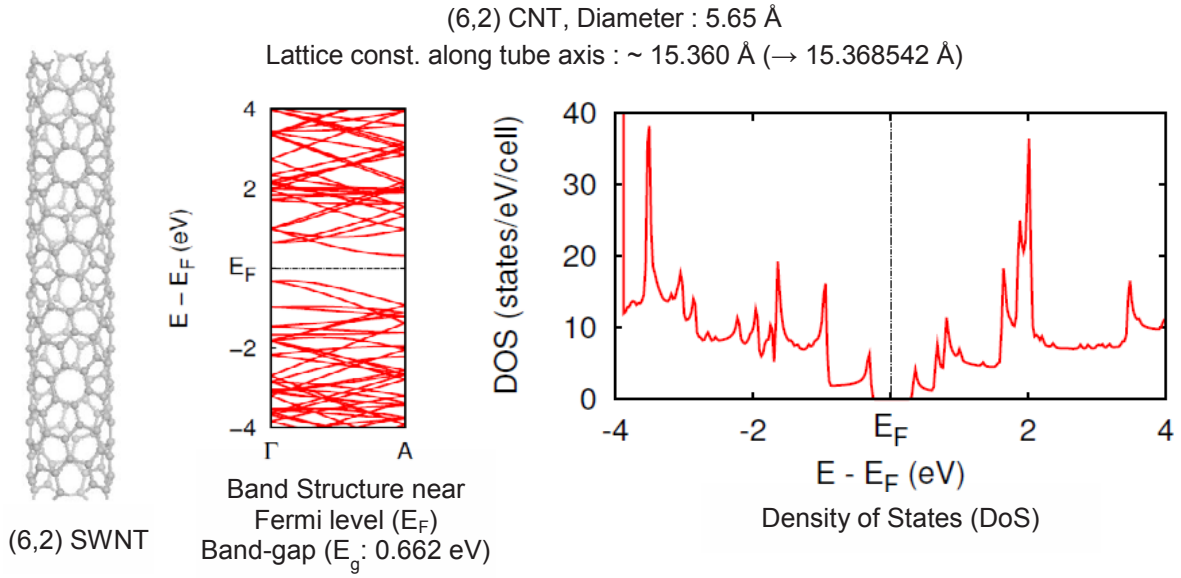

Figure S4.2: *Calculated Band structure and density of states of an isolated semiconducting (6,2) SWNT*

We used generalized gradient approximation (GGA)[11] functional by Perdew, Burke, and Ernzerhof (PBE)[12] for exchange-correlation functional and Troullier-Martins type norm-conserving pseudopotentials[13]. An atomic orbital basis with a double-ζ polarization was used to expand the electronic wave functions. A 200 Ryd mesh cutoff was chosen and the self-consistent calculations are performed with a mixing rate of 0.05. The convergence criterion for the density matrix is taken as 10^{-4}. The conjugate gradient method[14] was used to relax the atoms until the

maximum absolute force was less than 0.05 (eV/Å). We use the p(4x2) reconstruction of the Si(100) surface for substrate structure of semiconducting SWNTs. The Si portion of the system was treated as a bulk with a thin native oxide layer that prevented any bond-formation with the SWNTs. As discussed in the previous section, this oxide layer, if present, provided a possible tunneling barrier and our junction model takes this into account in the next subsection. In addition, we have also separately performed calculations where a (6,2) SWNT gets absorbed on the surface of Si. To do this, a slab with 7 silicon monolayers was used and the bottommost layer was hydrogen (H) terminated. Except the bottom Si 2-layers, all the atoms were fully relaxed with several types of buckled Si structures at the surfaces. We found the most stable p(4x2) Si(100) surface structures and calculated their electronic band structure with k-grid 12x24x1. The lattice constant of Si(100) slab along x-axis(longer, p4x2) was 15.3685Å, and the bandgap was 0.416 eV. By comparing with the band structure of Si(100) bulk and surface structure, we confirmed that the band dispersion near the Fermi level of Si(100) surface was due to the surface structure which resulted in reduced band gap from ~1.1 eV to 0.416 eV. The vacuum region in the vertical direction (z-axis) was at least 10Å with adsorption of SWNTs on the Si(100) surface to ignore the interaction between periodic images. We also considered the slab dipole-correction to introduce a dipole layer in the vacuum region to compensate the system dipole. The decrease of the band-gap occurs at an atomically narrow region of the junction and is unlikely to affect the injection of carriers from the Si to the SWNT electrodes. Further the possibility of such nanotubes to remain aligned and hence bonded with Si is low, and hence we have presented the more likely scenario in our analysis in section S4b, where the Si surface is coated with a thin tunneling oxide layer.

S4b. Semi quantitative modeling of the SWNT electrodes: We employ a simple model to describe the effective electronic structure of the SWNT belts as electrodes (layer c of figure S4.1b). Since the as-received SWNTs had d≈1nm, we assume that the belts contain an equal distribution of all chiralities (m,n) with d≈1nm. The cumulative DoS (CDoS) of the SWNT belts can be assumed to be proportional to an equally weighted sum of the individual DoS[15] of each chiral type, $CDoS = \Sigma_{m,n} D_{m,n}(\varepsilon)$. Here, ε=0 eV is the Fermi level, assumed to be the same for all SWNTs for the sake of simplicity. Since the diameter of the SWNTs were mostly between 0.9

DOI: 10.1038/NPHOTON.2014.1

and 1.1 nm, we chose all SWNT chiralities that corresponded to theoretical diameters ranging between 0.9 and 1.1 nanometers, that resulted in 22 chirality values used. Figure S4.3 shows the cumulative DoS (CDoS) of SWNTs (obtained by summing the DoS of 22 different chirality values of SWNTs with d≈1nm as shown), as a function of electronic energy, ε. Also shown is the

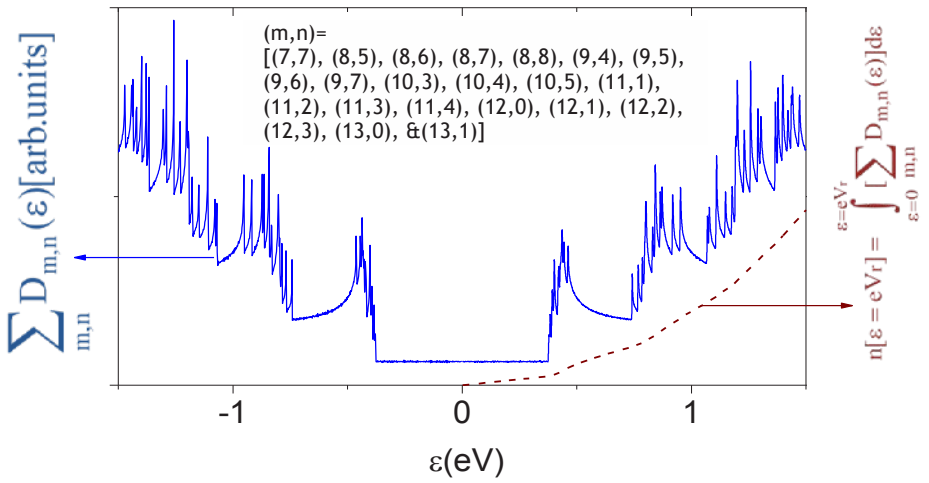

Figure S4.3: *Cumulative DoS (CDoS=$\Sigma_{m,n} D_{m,n}(\varepsilon)$) of selected d≈1nm SWNTs (with chirality values (m,n) as shown). The number of accessible states in SWNTs, $n[eV_r] = \int CDoS(\varepsilon)d\varepsilon$, integrated between ε=0 and ε=eV_r (V_r = reverse bias), as also shown (see text).*

number of accessible states above the Fermi level, as discussed later.

We next propose that the intermediate layer (layer b) is narrow, and hence the carrier injection through this layer is not going to be significantly affected by the actual layer of SWNTs that form this interface, and hence we can choose the (6,2) SWNT as a typical SWNT sandwiched between the electrode and silicon (with a native oxide layer). Past works have shown[16,17] that strong electric field gradients can potentially change the band structure and hence DoS of the SWNTs. However, for any significant modifications to the electronic structures the field-gradients need to be extremely high (**E** > a few Volts per nanometer). It is possible that the SWNTs which are in close proximity of the junction do experience high electric field-gradients that may potentially distort their electronic structure. However, such layers would be extremely narrow, and their exact DoS structures would not affect the total number of accessible states which lie further away into the main body of the SWNT belt (where the field gradient **E** is significantly smaller). We also note that since $n[eV_r]$ is an integral of the $CDoS(\varepsilon)d\varepsilon$, and the

CDoS contains a contribution from such a large number of chiralities, the non-linear and sharply rising shape of $n=n[eV_r]$ begins to become insensitive to the exact DoS structures. Hence, for ease of calculations, we have used the "zero-bias" DoS, shifted in a manner analogous to conventional p-n junctions. Although it does not take into account all the nuances of this system, we feel that it does help us understand why the photocurrent response in these junctions behave so differently from other conventional p-n junctions, even though the dark current-voltage relation behave conventionally.

Figure S4.4 shows the combined electronic structure of the SWNT electrode, a (6,2) SWNT, and its junction with Si (with a native oxide layer) under the application of a reverse bias. The band gaps at various regions have been schematically represented from the values discussed earlier. Our analysis shows that the oxide layer has little or no resistance to the junction, and possibly allows the carriers to tunnel through. The semiconducting (6,2) SWNT forms an ultrathin, nearly-metallic junction through which photoexcited carriers can easily penetrate, travels through a very short distance (possibly a few nanotube's width) before it arrives at the SWNT electrode area. The schematic also shows how the CDoS of the SWNT electrode shifts towards lower energy values due to an applied reverse bias V_r. The Fermi level of SWNTs gets lowered by an amount equal to the reverse bias V_r, with respect to its original position near the CBE of of Si, as discussed in the main text. As a result, under this applied reverse bias, the Fermi level and hence the number of electron-occupied states of the SWNT belt move to lower energies, opening up accessible states for photoexcited electrons to inject from Si into the SWNTs. From the CDoS, the total number of accessible states, $n(V_r)$, is calculated as:

$$n(\varepsilon = eV_r) = \int_{\varepsilon=0}^{\varepsilon=eV_r} [\sum_{m,n} D_{m,n}(\varepsilon)] d\varepsilon$$

DOI: 10.1038/NPHOTON.2014.1

The variation of n=n(eV$_r$) as a function of V$_r$ has been plotted in figures S4.3, S4.4 as well as in

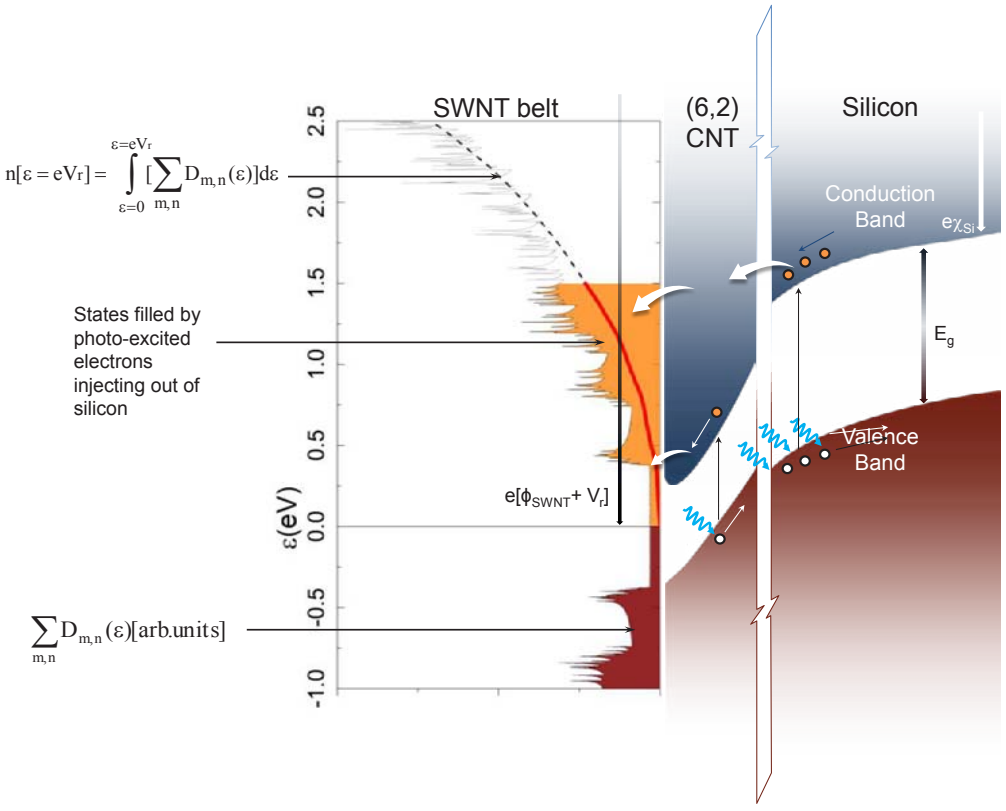

Figure S4.4: *Schematic energy-level diagram of Si with a tunneling oxide barrier undergoing photoexcitation, adjacent to a narrow layer of (6,2) SWNTs, followed by the cumulative DoS (CDoS=$\Sigma_{m,n} D_{m,n}(\varepsilon)$) of selected d≈1nm SWNTs (with chirality values (m,n) as shown in figure S1.6). The photocurrent (corresponding to the carriers shown in yellow) is due to injected electrons from Si into SWNTs and is limited by the (reverse bias dependent) number of accessible states in SWNTs, n[eV$_r$] =∫CDoS(ε)dε, integrated between ε=0 and ε=eV$_r$(V$_r$=*

figure 1d inset for comparison with the measured photocurrent. It can be seen that despite the simple approach of this model, the shape of n=n(eV$_r$) is quite consistent with that of our experimental photocurrent data, suggesting that the SWNT DoS plays a key role in determining the photocurrent response in these devices. We believe that a more accurate description of the CDoS, incorporating the atomistic interaction[18] between SWNT/Si and SWNT/SWNT junctions (sidewall and end-end) can result in more quantitative insight of the behavior of these junctions.

S4c: Origin of symmetric photocurrent in the bi-directional phototransistor (figure 3b): The phototransistor is essentially two back-to-back SWNT/Si photodiodes as mentioned in the main manuscript, and can be schematically described as seen in figure S4.5a.

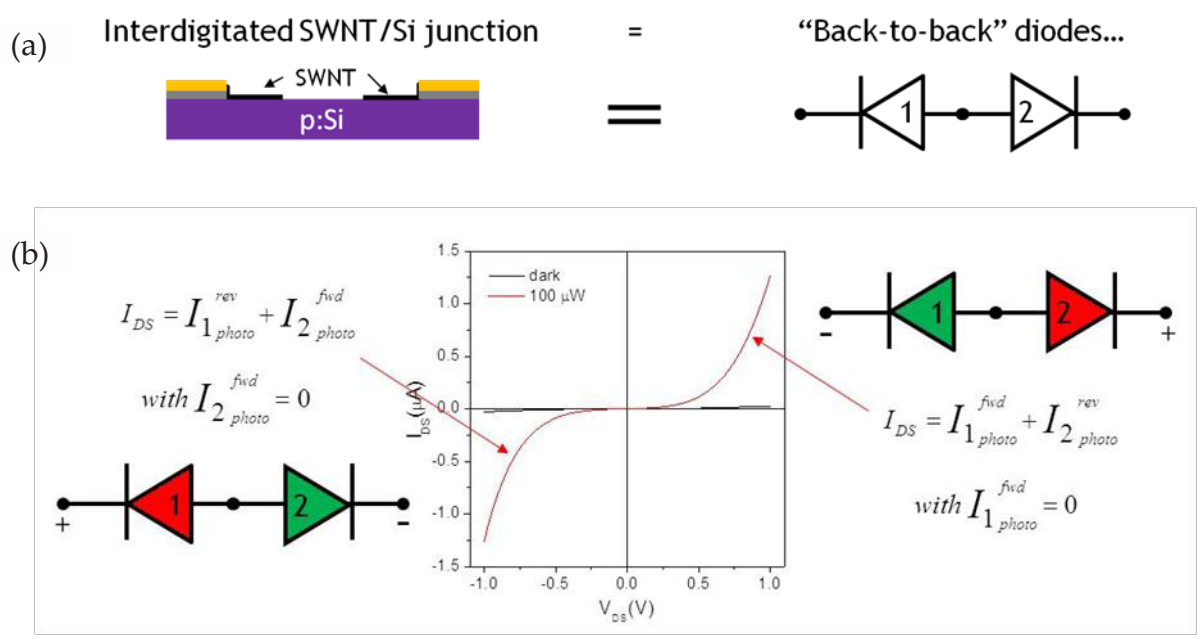

Figure S4.5: *(a) Schematic and equivalent circuit representation of the bi-directional phototranistor. (b) Schematic showing its operation in the first and third quadrant in dark and illuminated conditions.*

Under illumination, the diode in the reverse bias generates a photocurrent and the one in the forward bias conducts but generates no photocurrent. This situation can be schematically described as shown in figure S4.5b. In the first quadrant, diode 2 generates photocurrent and diode 1 conducts, and in the third quadrant, it is the other way around. Since the two diodes are mirror-symmetric, $I_{1\,photo}^{rev}(V) = -I_{2\,photo}^{rev}(-V)$.

S5: Logic device characterizations: The current density was measured as a function of various (broadband and monochromatic) incident powers. The spectral dependence of the broadband source is shown in figure S5.1.

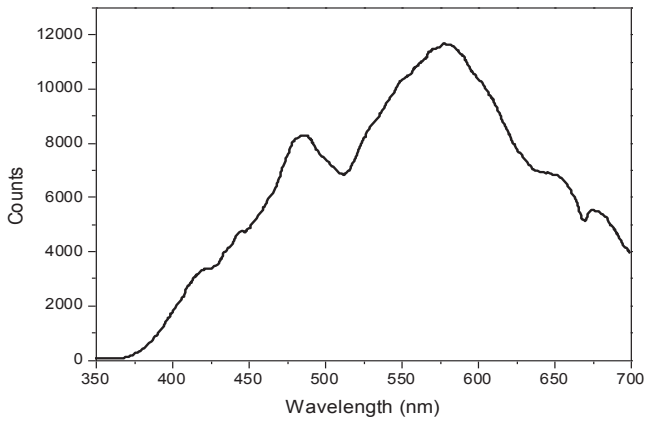

Figure S5.1: *Spectral characteristics of the broadband source referred to in the main manuscript*

DOI: 10.1038/NPHOTON.2014.1

Figure S5.2a shows the variation of dark and photo-induced current-densities as a function of applied voltage, measured in the same device shown in figure 1.

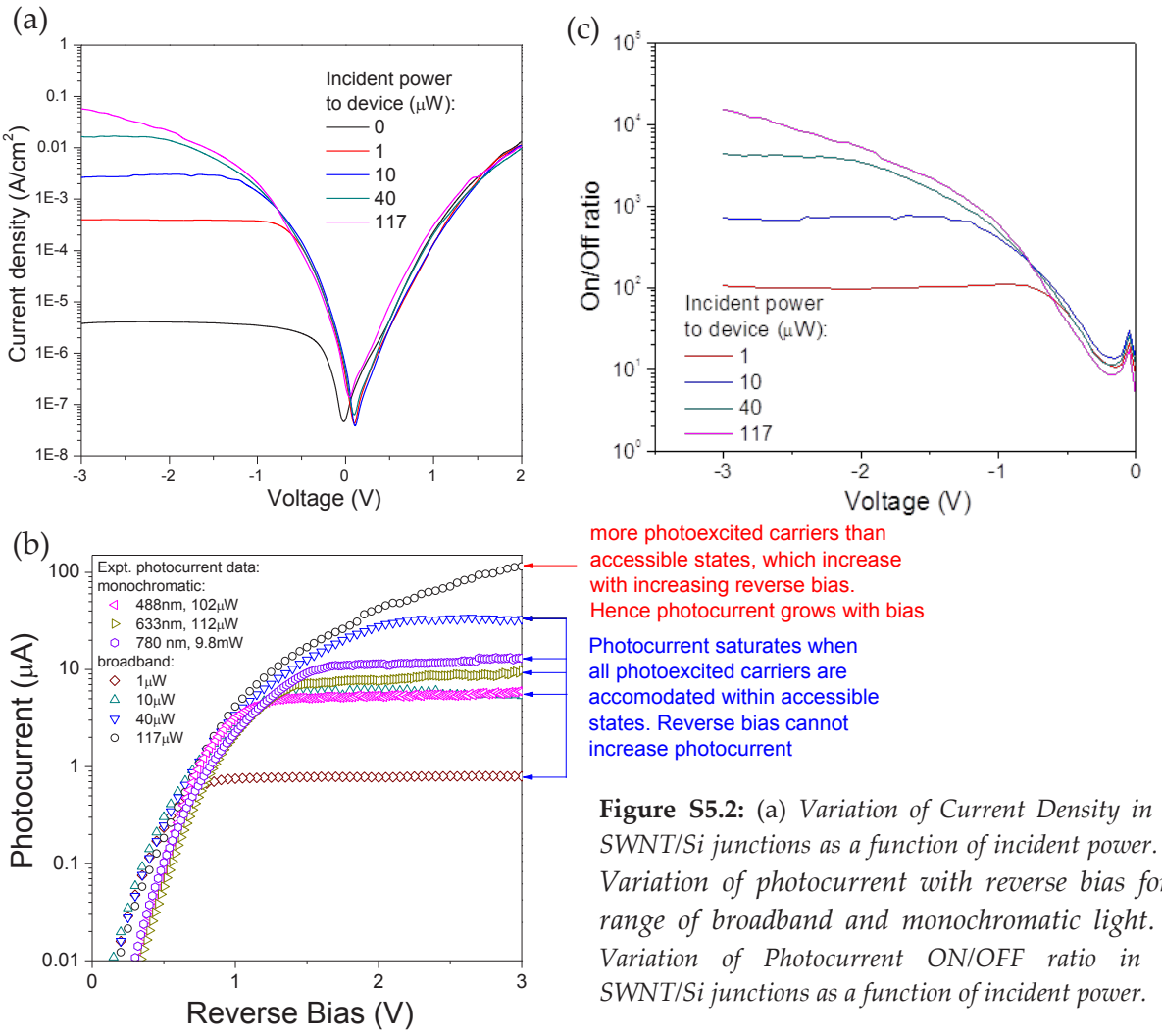

Figure S5.2: (a) *Variation of Current Density in the SWNT/Si junctions as a function of incident power. (b) Variation of photocurrent with reverse bias for a range of broadband and monochromatic light. (c) Variation of Photocurrent ON/OFF ratio in the SWNT/Si junctions as a function of incident power.*

At the highest applied incident power, the shape of the Photo I-V curve is almost mirror symmetric with respect to the applied bias on two sides of current minimum point, which indicates that the voltage-induced forward current and the photo-induced reverse current are both limited by similar SWNT DoS, which is a natural outcome of the fact that the DoS of SWNTs are theoretically mirror-symmetric about the Fermi level, as seen in figure S4.3. At lower power values, the reverse-bias currents follow the same curves at lower bias, and then saturates to a constant value at higher biases. This has been plotted in greater detail in figure S5.2b, which shows the variation of the (dark-current-subtracted) photocurrent as a function of the reverse bias, for monochromatic as well as a broadband source of varying powers.

Irrespective of the incident light, the low-(reverse)-bias photocurrent follows the same curve, where the photocurrent is limited by the number of accessible states, and hence photocurrent is reverse-bias dependent. At higher biases, the photo-excited carriers all have accessible states to inject into, and hence the photocurrent saturates beyond a certain value of reverse-bias values. The interplay of number of photo-excited carriers and number of accessible states at different incident bias values is clearly seen here. The ON/OFF ratio is also dependent on the bias and incident powers, as seen in figure S5.2c. At a reverse bias value of V_r=-3V and at the highest incident power, the ON/OFF ratio I^{max}/I^{min} exceeds 10^4. As a measure of its performance over a range of incident powers, we can define the current dynamic range of this device, $\mathrm{CDR(dB)} = 20\log[\frac{I^{\max}}{I^{\min}}]$, exceeds 80dB.

The switching speed and pulse width of these devices were obtained by characterizing the time-domain response of these devices in an oscilloscope when illuminated by a optically chopped laser signal. A 488nm laser was chopped at 1000 Hz which is the highest chopping speed of our instrument. Figure S5.3 summarizes the switching response of the logic devices.

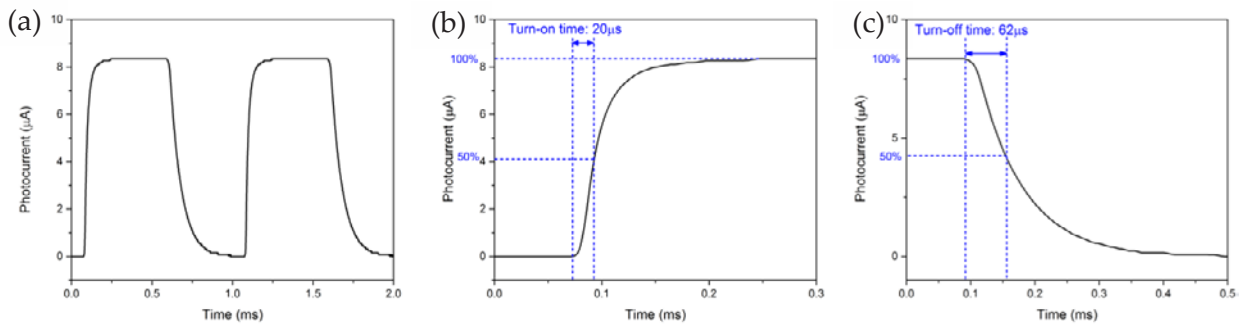

Figure S5.3 *(a) Photocurrent response to an optically chopped laser source, as a function of time. Calculation of (b) rise (laser ON) time and (c) fall (laser OFF) switching time scales.*

The opening (and closing) time of the chopper is about 20 μs at 1000 Hz. For the photocurrent device, the half-maximum rise-time (when the chopper opens) equals to 20μs, implying that the switching speed is faster than 20μs. The half-maximum fall-time (at the closing of the chopper) is about 62μs.[Footnote3] If we assume that the rise-time is comparable to the chopping speed, the

Footnote 3: This comparatively larger fall-time could be a result of the slower recombination rate of carriers in silicon, see Solid-State Electronics 26, 577-597 (1983).

DOI: 10.1038/NPHOTON.2014.1

minimum pulse width can be obtained by taking the sum of half-maximum rise-time and fall-time time which is about 82μs, from which we define the effective switching speed as 1/82μs = 12kHz. We note that the power consumed per pulse depends on the photocurrent, which in turn depends both on incident light power and reverse bias. For the device in figure S5.3, the power consumed per pulse was (obtained by averaging $I_{ph}(t)\times V_r$ over an entire pulse) ≈ 2.6 μW. We note that the faster rise-time indicates that the carrier excitation and injection into the SWNTs is faster than our measurement limits, which is quite an encouraging result. The fall-time may improve substantially if the doping levels of silicon adjusted for faster recombination rates. Improving the process-steps that could potentially prevent the formation of native oxides may also improve the switching time-scales. This would greatly benefit their integration into more realizable devices. We further note that these switching speeds are quire sufficient for imaging applications.

S6. Photo-detector Array Characterizations: The following section presents characterization data for the photodetector array.

S6.1 Photocurrent Map: In order to analyse the pixel-performance reproducibility of our photodetector array, a photocurrent map was measured over 25 pixels (5x5) in the device shown in figure S2.3. The corresponding lateral size ≈ 125 microns in each direction, and scan sizes beyond this caused the laser spot to go out of focus due to unavoidable stage tilt. The photoexcitation was performed using a laser beam of wavelength of 488nm and incident power of 260 μW, focused to a spot of size ~1 micron using a 100x microscope objective and modulated by an optical chopper at 1000Hz. The device was in series with a 46 kΩ resistor and biased at -2 V. The electrical signal was detected by a lock-in amplifier and was converted into photocurrent (nA). Figure S6.1a show the photocurrent map. The histogram of the average photocurrent of each pixel is plotted in figure S6.1b, with bin size of 10 nA. The mean photocurrent was found to be = 256±13nA, *i.e.* the variation of photocurrent was about 10%.

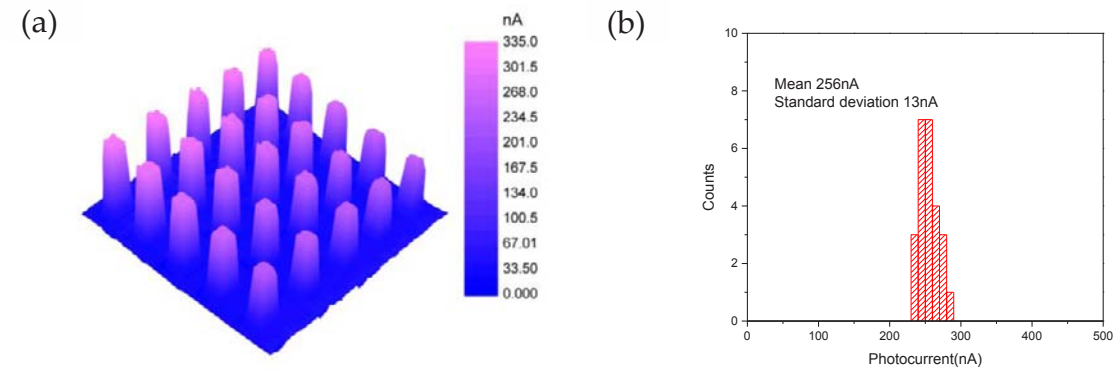

Figure S6.1: (a) *Photocurrent map of 25 pixels from a pixel-array detector test structure. (b) Histogram of the average current showing mean and standard deviation.*

S6.2 Linearity and current Dynamic Range: The photocurrent was measured in a typical pixel as a function of incident power at a reverse bias of -3V using a tunable incident laser of wavelength λ=488nm. Figure S6.2a shows the linearity of this pixel over four decades of incident power. In this case, we define the current dynamic range as $\mathrm{CDR(dB)} = 20\log[\frac{I_{850\mu W}}{I_{dark}}]$ ≈90dB (using values shown in figure S6.2). The corresponding dark current density is about 20 mA/cm^2. Unfortunately, since the underlying Si is a single large wafer, we could not isolate each "pixel" optically from each other to obtain any meaningful estimate of the crosstalk.

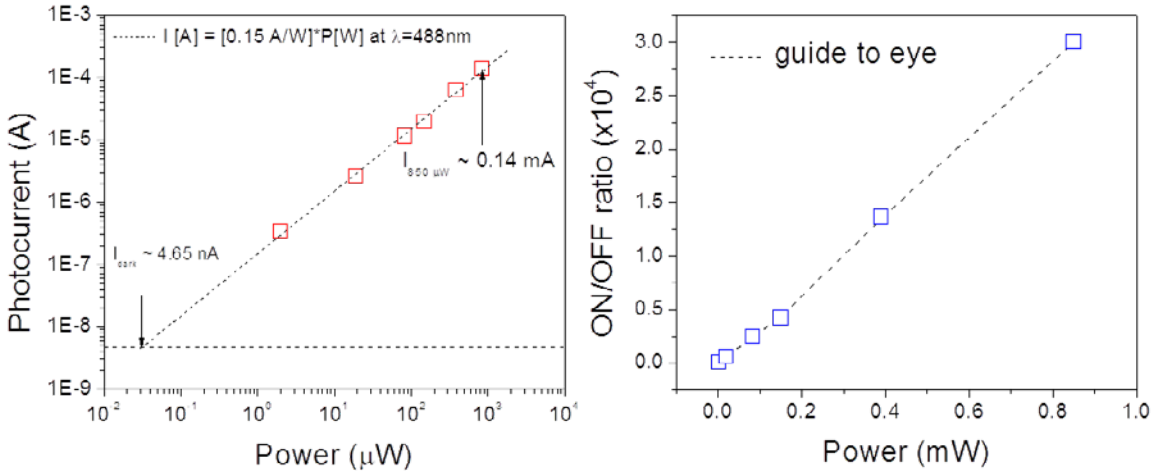

Figure S6.2: (a) *Pixel photocurrent response, demonstrating linearity over several decades of incident power at -3V. The data was measured using a monochromatic source of λ=488 nm. (b) ON/OFF ratio as a function of power in the same device.*

DOI: 10.1038/NPHOTON.2014.1

S7. A list of other optical switching mechanisms with some related published works:

A. All-optical Switching approaches:

Year	Optically active system/technique	Switching behaviour	Possible applications	Current Integration compatibility	Reference
2013	Molasses of ^{133}Cs atoms in a MOT-trap at 35μK	Several hundred photons/ gate photon	Quantum information processing	Ultra-low temperature applications	Ref.[19]
2010	EM radiation controlled cavity resonance at cryogenic temperatures	Heterodyne signal modulation of ~500	On chip quantum information processing and photonics	Ultra-low temperature applications	Ref.[20]
2009	Population inversion in a single molecule at T=1.4K	Transmittance changes from 93% to 100% under 10μW incident laser	Quantum information processing	Low-temperature applications	Ref.[21]

B. Optoelectronic Switching approaches:

	Optically active system/technique	Responsivity	Possible applications	Current Integration compatibility	Reference
2013	SWNT/Si Schotty-type junctions	1 A/W broadband, 10^5 V/W	Tunable Photoswitch, Imaging devices, Optoelectronic Logic Circuits.	Room Temperature	Current work
2011	Graphene	5 mA/W at low temperature, λ = 850nm, $V_{Backgate}$ = -5V, $V_{Topgate}$=2V, V_{SD}=0V.	Photodetectors, solar energy harvesting	Room Temperature down to 10K	Ref.[22]
2011	Graphene	1.5 mA/W, λ = 532 nm, V_{gate} = -10 V, V_{SD} = 10 mV.	Bolometers, Pixilated infrared imaging	Room temperature	Ref.[23]
2011	MWNTs on polymide substrate	1200V/W, V_{SD} = 0.2 mV	IR detectors, Bolometers	Compatible with polymer substrate, vacuum condition preferred (sensitive to humidity)	Ref.[24]
2010	Graphene	6.1 mA/W, λ = 1550 nm, V_{SD} = 0.4 V, V_{gate} = -15 V.	Optical communications	Room temperature	Ref.[25]
2009	Ge on Si	1.1A/W, V_{SD} = -1V, λ = 1550nm.	Photodetectors	CMOS compatible	Ref.[26]
2009	SWNTs	250V/W (room temperature), 2000V/W(T = 90K), I_{bias} = 5 mA, radiation 0.3 mW/mm.	Bolometers	Bolometric detection	Ref.[27]
2008	GaNAsSb	12A/W, λ = 1300nm V_{SD} = ~4.8V	IR detectors		Ref.[28]
2008	Ge on Si	0.85A/W , λ = 1550nm, V_{SD} = -1V	Photodetectors	CMOS compatible	Ref.29
2008	SWNTs	1500V/W, λ = 11.3 and 20 μm, T = 28K.	IR detectors	Low temperature	Ref.[30]
2007	Ge on Si	1A/W, λ =1550nm, with 2% variation when V_{SD} =	Photodetectors	CMOS compatible	Ref.[31]

2007	AlGaInAs on Si	1V to 7 V. 1.1/W, λ = 1550nm, V_{SD} = -2V.	Photodetectors	CMOS compatible	Ref. [32]
2006	Ge on Si	1A/W, λ = 1520nm, V_{SD} = -1V.	Photodetectors	CMOS compatible	Ref.[33]

λ: excitation wavelength, V_{SD}: source and drain voltage, V_{gate}: gate voltage, I_{bias}: bias current, T: temperature
Note: the structures of devices and the sensing mechanisms are different. Therefore, the measurement conditions will be different.

C. Optoelectronic Logic devices

Year	Optically active system/technique	Responsivity	Possible applications	Current Integration compatibility	Reference
2010	Cadmium sulfide (CdS)/ITO		Optical to electrical signal processing	Thin films	Ref.[34]
1994	GaAs		Optical to electrical signal processing	CMOS compatible	Ref.[35]

References

1 Kim, Y. L., Jung, H. Y., Kar, S. & Jung, Y. J. Cleaning organized single-walled carbon nanotube interconnect structures for reduced interfacial contact resistance. *Carbon* **49**, 2450-2458 (2011).

2 Okpalugo, T., Papakonstantinou, P., Murphy, H., McLaughlin, J. & Brown, N. High resolution XPS characterization of chemical functionalised MWCNTs and SWCNTs. *Carbon* **43**, 153-161 (2005).

3 Estrade-Szwarckopf, H. XPS photoemission in carbonaceous materials: A "defect" peak beside the graphitic asymmetric peak. *Carbon* **42**, 1713-1721 (2004).

4 Ghosh, S., Bachilo, S. M. & Weisman, R. B. Advanced sorting of single-walled carbon nanotubes by nonlinear density-gradient ultracentrifugation. *Nature Nanotech.* **5**, 443-450 (2010).

5 Jaber-Ansari, L. *et al.* Mechanism of Very Large Scale Assembly of SWNTs in Template Guided Fluidic Assembly Process. *J. Am. Chem. Soc.* **131**, 804-808 (2009).

6 Xiong, X., Jaberansari, L., Hahm, M., Busnaina, A. & Jung, Y. Building highly organized single-walled-carbon-nanotube networks using template-guided fluidic assembly. *Small* **3**, 2006-2010 (2007).

7 Kim, Y. L. *et al.* Highly Aligned Scalable Platinum-Decorated Single-Wall Carbon Nanotube Arrays for Nanoscale Electrical Interconnects. *ACS Nano* **3**, 2818-2826 (2009).

8 Groning, O., Kuttel, O. M., Emmenegger, C., Groning, P. & Schlapbach, L. Field emission properties of carbon nanotubes. *J. Vac. Sci. Technol. B* **18**, 665-678 (2000).

9 Ruffieux, P. *et al.* Hydrogen adsorption on sp(2)-bonded carbon: Influence of the local curvature. *Phys Rev B* **66** (2002).

10 Soler, J. M. *et al.* The SIESTA method for ab initio order-N materials simulation. *J. Phys-Condens. Mat.* **14**, 2745-2779 (2002).

11 Perdew, J. P. & Yue, W. Accurate and Simple Density Functional for the Electronic Exchange Energy - Generalized Gradient Approximation. *Phys Rev B* **33**, 8800-8802 (1986).

12 Perdew, J. P., Burke, K. & Ernzerhof, M. Generalized gradient approximation made simple. *Phys Rev Lett* **77**, 3865-3868 (1996).

13 Troullier, N. & Martins, J. L. Efficient Pseudopotentials for Plane-Wave Calculations. *Phys Rev B* **43**, 1993-2006 (1991).

14 Hestenes, M. R. & Stiefel, E. Methods of Conjugate Gradients for Solving Linear Systems. *J. Res. Nat. Bur. Stand.* **49**, 409-436 (1952).

DOI: 10.1038/NPHOTON.2014.1

15 Saito, R., Dresselhaus, G. & Dresselhaus, M. S. Trigonal warping effect of carbon nanotubes. *Phys Rev B* **61**, 2981-2990 (2000).

16 Kim, C., Kim, B., Lee, S. M., Jo, C. & Lee, Y. H. Electronic structures of capped carbon nanotubes under electric fields. *Phys Rev B* **65**, 165418 (2002).

17 Mouri, M., Ogawa, M. & Souma, S. Influence of geometrical deformation and electric field on transport characteristics through carbon nanotubes. *J. Appl. Phys.* **112**, 114328-114328-114325 (2012).

18 Kwon, Y. K., Saito, S. & Tomanek, D. Effect of intertube coupling on the electronic structure of carbon nanotube ropes. *Phys Rev B* **58**, 13314-13317 (1998).

19 Chen, W. *et al.* All-Optical Switch and Transistor Gated by One Stored Photon. *Science* **341**, 768-770 (2013).

20 Weis, S. *et al.* Optomechanically Induced Transparency. *Science* **330**, 1520-1523 (2010).

21 Hwang, J. *et al.* A single-molecule optical transistor. *Nature* **460**, 76-80 (2009).

22 Gabor, N. M. *et al.* Hot Carrier-Assisted Intrinsic Photoresponse in Graphene. *Science* **334**, 648-652 (2011).

23 Lemme, M. C. *et al.* Gate-Activated Photoresponse in a Graphene p-n Junction. *Nano Lett.* **11**, 4134-4137 (2011).

24 Gohier, A. *et al.* All-printed infrared sensor based on multiwalled carbon nanotubes. *Appl Phys Lett* **98** (2011).

25 Mueller, T., Xia, F. N. A. & Avouris, P. Graphene photodetectors for high-speed optical communications. *Nature Photon.* **4**, 297-301, doi:Doi 10.1038/Nphoton.2010.40 (2010).

26 Feng, D. Z. *et al.* High-speed Ge photodetector monolithically integrated with large cross-section silicon-on-insulator waveguide. *Appl Phys Lett* **95** (2009).

27 Lu, R. T., Li, Z. Z., Xu, G. W. & Wu, J. Z. Suspending single-wall carbon nanotube thin film infrared bolometers on microchannels. *Appl Phys Lett* **94** (2009).

28 Tan, K. *et al.* High responsivity GaNAsSb pin photodetectors at 1.3 μm grown by radio-frequency nitrogen plasma-assisted molecular beam epitaxy. *Opt Express* **16**, 7720-7725 (2008).

29 Masini, G., Sahni, S., Capellini, G., Witzens, J. & Gunn, C. High-speed near infrared optical receivers based on Ge waveguide photodetectors integrated in a CMOS process. *Adv. Opt. Tech.* **2008** (2008).

30 Itkis, M. E., Yu, A. P. & Haddon, R. C. Single-walled carbon nanotube thin film emitter-detector integrated optoelectronic device. *Nano Lett.* **8**, 2224-2228 (2008).

31 Vivien, L. *et al.* High speed and high responsivity germanium photodetector integrated in a Silicon-on-insulator microwaveguide. *Opt Express* **15**, 9843-9848 (2007).

32 Park, H. *et al.* A hybrid AlGaInAs-silicon evanescent waveguide photodetector. *Opt Express* **15**, 6044-6052 (2007).

33 Liu, J. *et al.* in *Group IV Photonics, 2006. 3rd IEEE International Conference on.* 173-175 (IEEE).

34 Mech, J., Kowalik, R., Podborska, A., Kwolek, P. & Szacilowski, K. Arithmetic Device Based on Multiple Schottky-like Junctions. *Aust. J. Chem.* **63**, 1330-1333 (2010).

35 She, T. & Shu, C. in *Electron Devices Meeting, 1994. Proceedings., 1994 IEEE Hong Kong.* 54-57 (IEEE).